Investigating Subglacial Quarrying with Rock Fracture Simulations

William J. Bertrand

Senior Honors Thesis

Department of Physics and Astronomy

Oberlin College

March 31, 2021

Acknowledgements

Abstract

We use the extended finite element method to conduct fracture simulations of glacially loaded bedrock, with the aim of better understanding the erosive process of quarrying. In quarrying, cavity formation over bedrock obstacles creates deviatoric stresses that drive fractures to propagate and isolate bedrock blocks, which are then carried away by the overriding ice. Existing literature assumes straight-line, bed-normal fracture growth as an adequate approximate solution to an idealized model problem, which we show to be highly inaccurate via numerical solutions to the same problem. We show that bedrock ledges create high concentrations of stress at their boundaries, which drives curved fracture propagation at much higher rates than previously predicted.

Contents

List of Figures

Chapter 1

Introduction

The influence of glaciers in shaping landscapes is well-known to specialists and travelers alike – both the rough, extreme topography of places like western Norway and the smooth, rolling topography of the American midwest mark the pronounced erosive impact of ice sheets and glaciers. The scientific study of glaciers is only about a century old, and quantitative study of the processes driving erosion, which occur in difficult-to-reach places buried under kilometers of ice, is only emerging in recent decades. The pronounced results of subglacial erosion are widely known, but scientists still lack a detailed understanding of these erosive processes.

Evidence, such as glaciated bedrock and glacial outwash (the debris in meltwater at the foot of glaciers), indicates that two main processes are responsible for subglacial erosion – abrasion, wherein hard debris frozen into the ice is dragged over the bedrock, creating remarkably smooth rocks with "glacial polish" as well as striations and chattermarks; and quarrying, wherein the pressure exerted by the ice causes fractures to propagate through bedrock obstacles, eventually isolating (or "plucking") bedrock blocks (rock fragments in figure 1.1), which are then frozen into in the ice flow to be taken along with the glacier, inevitably causing abrasion on the way down.

Figure 1.1: Heavily quarried bedrock in front of Castleguard glacier in Switzerland, showing sharp step ledges in natural bedrock, with a classic stepped bed geometry. Note that this bedrock is exposed from recent glacier retreat, and thus also shows heavy plucking (quarrying) of the step ledges in the photo, with loose, glacially-extracted rock fragments covering the area. Red boxed region shows a series of steps akin to our model problem. Photo courtesy of Jacob Woodard and Luke Zoet.

In this study, we go through the necessary background in the physics of solids and fractures, as well as the methods required for the simulation of fracture, in order to present the most detailed small-scale model of subglacial quarrying to date. These simulations are undertaken in order to improve estimates of quarrying rates and understanding of subglacial processes, since a recent study [1] revealed significant shortcomings in the traditional approach to the problem [2].

Chapter 2

Theory

2.1 Solid Mechanics, Continuum Mechanics

For most purposes in classroom mechanics, solid objects are reduced to some simplified set of coordinates – center of mass and rotational angle, with some moment of inertia, or approximated as a simple point source, etc. – but when looking to study the deformation or failure of an arbitrary solid, a continuum approach must be taken.

2.1.1 Stress

This continuum approach uses a tensor formulation to describe all forces acting on an infinitesimal of our solid dm. Restricting our attention to two-dimensional problems, we use the Cauchy stress tensor

$$\boldsymbol{\sigma} = \begin{pmatrix} \sigma_{xx} & \tau_{xy} \\ \tau_{xy} & \sigma_{yy} \end{pmatrix} \tag{2.1}$$

to describe the state of forces for a point in our solid, where a force per unit area (called a traction) $\vec{F}$ which acts on a plane with unit normal vector $\hat{n}$ is given as

$$\vec{F} = \boldsymbol{\sigma}\hat{n} = \begin{pmatrix} \sigma_{xx} & \tau_{xy} \\ \tau_{xy} & \sigma_{yy} \end{pmatrix} \begin{pmatrix} n_x \\ n_y \end{pmatrix} = \begin{pmatrix} \sigma_{xx}n_x + \tau_{xy}n_y \\ \tau_{xy}n_x + \sigma_{yy}n_y \end{pmatrix}. \tag{2.2}$$

Note that even though $\vec{F}$ in equation (2.2) acts against a specified plane, $\vec{F}$ is still a vector quantity. This is because a traction can act normal to the plane (normal stress), or it can

act parallel to the plane (shear stress). In the case where $\hat{n}$ lies along our axes, the resulting shear and normal stresses are depicted in figure (2.1b). The stress tensor is symmetric (see [3] for a proof), so $\tau_{xy} = \tau_{yx}$. For an arbitrary $\hat{n}$, the traction is depicted in figure (2.1a), where $\vec{F} \cdot \hat{n}$ and $||\vec{F} \times \hat{n}||$ are the normal and shear components along $\hat{n}$, respectively.

(a)   (b)
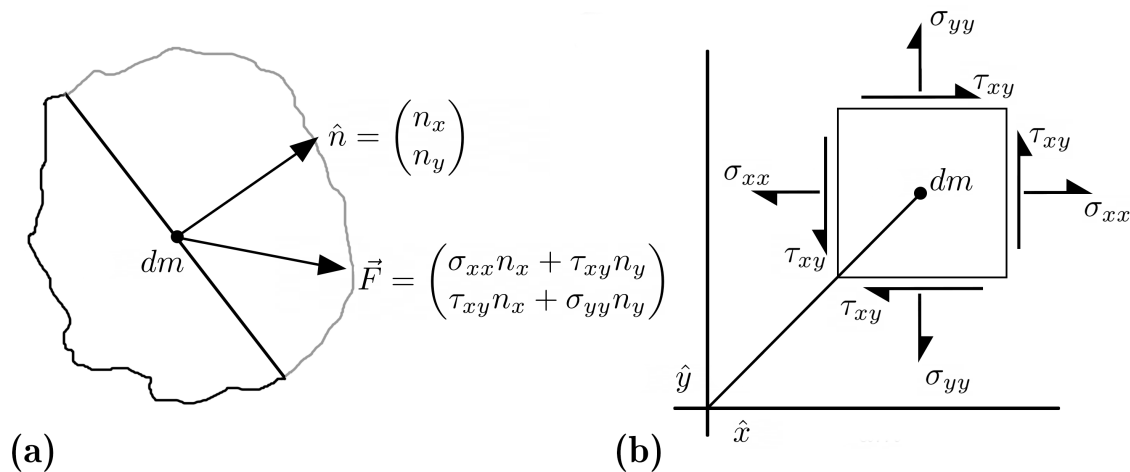
Figure 2.1: (a) fictitious $\hat{n}$ within a solid and the resulting traction. (b) normal and shear tractions in terms of the stress tensor at a point dm.

While we only have a single $\hat{n}$ along the boundary of our solid, and thus only a single traction vector at each point along our boundary, within the solid, our stress tensor $\boldsymbol{\sigma}$ describes a continuum of tractions which act for all possible $\hat{n}$. This continuum of tractions means that only $\boldsymbol{\sigma}$ can describe the balance of forces within our solid.

2.1.2 Displacement and Strain

In response to the tractions within a solid, our points dm_i at positions $\vec{x}_i$ undergo certain displacements to new positions $\vec{x}_i^*$, where we define the displacement as $\vec{u}(\vec{x}_i) = \vec{x}_i^* - \vec{x}_i$. In order to distinguish deformation (nonuniform displacement) from rigid motion (uniform displacement), we introduce a relative quantity related to displacement called strain ε, which is clearest to describe in one dimension.

If we have a bar of length L, the strain can be described as the fractional increase in

4
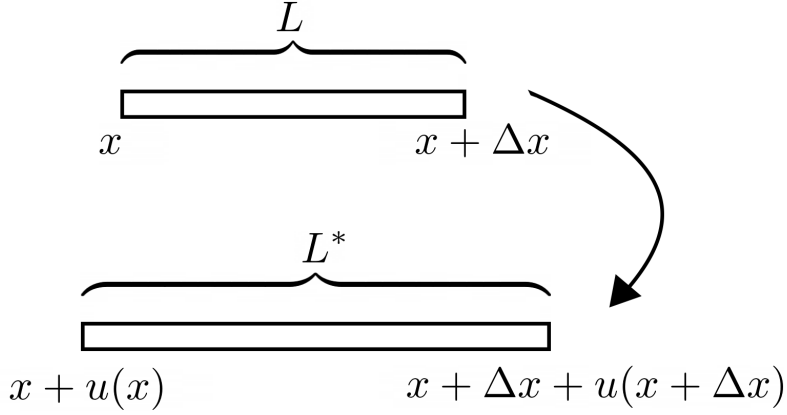
Figure 2.2: 1d bar of original length L and deformed length L^*

the length of the bar – looking at figure (2.2), we can describe this as

$$\varepsilon = \frac{L^* - L}{L} = \frac{[(x + \Delta x + u(x + \Delta x)) - (u(x) + x)] - [(x + \Delta x) - x]}{(x + \Delta x) - x}$$

$$= \frac{u(x + \Delta x) - u(x)}{\Delta x} = \frac{\Delta u}{\Delta x} \quad (2.3)$$

Taking the limit as $L \to 0$, we find $\varepsilon = du/dx$. Much like stress, strain in two dimensions is described is described by a symmetric tensor of the form

$$\varepsilon = \begin{pmatrix} \varepsilon_{xx} & \varepsilon_{xy} \\ \varepsilon_{xy} & \varepsilon_{yy} \end{pmatrix} = \begin{pmatrix} \frac{\partial u}{\partial x} & \frac{1}{2}\left(\frac{\partial u}{\partial y} + \frac{\partial v}{\partial x}\right) \\ \frac{1}{2}\left(\frac{\partial u}{\partial y} + \frac{\partial v}{\partial x}\right) & \frac{\partial v}{\partial y} \end{pmatrix} = \frac{1}{2}\left(\nabla \vec{u} + (\nabla \vec{u})^T\right), \quad (2.4)$$

where $\vec{u} \cdot \hat{x} = u$ and $\vec{u} \cdot \hat{y} = v$, and where we define the gradient of a vector to be a tensor:

$$\nabla \vec{u} = \begin{pmatrix} \frac{\partial u}{\partial x} & \frac{\partial u}{\partial y} \\ \frac{\partial v}{\partial x} & \frac{\partial v}{\partial y} \end{pmatrix}. \quad (2.5)$$

Note that the strain-displacement relation described in equation (2.4) is only valid for small, infinitesimal deformations [3].

2.1.3 Stress-Strain Relations

The stress tensor $\boldsymbol{\sigma}$ and the strain tensor $\boldsymbol{\varepsilon}$ are the continuum generalizations of force and displacement, respectively. To complete a picture of solid mechanics, however, we are

required to stipulate some relationship between stress and strain. The relationship chosen depends on the phenomena one would like to include in the model as well as the degree of (in-)homogeneity of the solid in question. These relationships are called a 'constitutive law' or 'material model'. A constitutive law is said to be linear elastic if the stresses are a linear combination of the strains, where in general this linear combination is given by a fourth-order tensor called the "stiffness tensor":

$$\boldsymbol{\sigma} = \boldsymbol{C} \colon \boldsymbol{\varepsilon} \qquad \text{or} \qquad \sigma_{ij} = \sum_{k,l} C_{ijkl} \varepsilon_{kl}. \tag{2.6}$$

Equation (2.6) is referred to as the continuum formulation of Hooke's law ($F = kx$). Instead of having a single spring constant k, in general $\boldsymbol{C}$ has 21 independent elastic moduli [4]. For our solid, we assume it is isotropic – that is, the stiffness of the material is direction independent. This reduces $\boldsymbol{C}$ to only two independent elastic moduli [4], which allows us to rewrite equation (2.6) in vector notation as

$$\boldsymbol{\sigma} = \lambda \mathbf{tr}(\boldsymbol{\varepsilon}) \boldsymbol{I} + 2\mu \boldsymbol{\varepsilon} \ \text{ or } \ \begin{pmatrix} \sigma_{xx} & \sigma_{xy} \\ \sigma_{xy} & \sigma_{yy} \end{pmatrix} = \lambda \begin{pmatrix} \varepsilon_{xx} + \varepsilon_{yy} & 0 \\ 0 & \varepsilon_{xx} + \varepsilon_{yy} \end{pmatrix} + 2\mu \begin{pmatrix} \varepsilon_{xx} & \varepsilon_{xy} \\ \varepsilon_{xy} & \varepsilon_{yy} \end{pmatrix}, \tag{2.7}$$

where λ and μ are two material stiffness parameters called the first Lamé parameter and the shear modulus, respectively. Thus our displacement-strain and strain-stress relationships mean that we can obtain $\boldsymbol{\sigma}$ from $\nabla \vec{u}$, and vice-versa, by substituting equation (2.4) into (2.7).

While we have defined equation (2.7) in terms of λ and μ, many other elastic moduli are in use, such as Young's modulus E, bulk modulus K, or Poisson's ratio ν. Any two of these parameters are sufficient to describe an isotropic solid's stiffness, and for the remainder of our study we will use the more popular Young's Modulus E and Poisson's ratio ν [1] instead of λ and μ, which are related to each other by [4]

$$E := \frac{\mu(3\lambda + 2\mu)}{\lambda + \mu}, \qquad \nu := \frac{\lambda}{2(\lambda + \mu)}. \tag{2.8}$$

---

[1] Young's Modulus is defined simply as stress over strain, which is linear below a material's yield stress, and Poisson's ratio is a measure of the extent to which a solid spreads out in response to uniaxial compression.

As a final note, we must stipulate some relationship between our two dimensional problem and the three-dimensional reality. The two most common relationships are plane stress, which assumes negligible out-of-plane stresses in a thin solid, such as a loaded plate; and plane strain, which assumes that the out-of-plane dimension of our solid is much larger than our x or y dimensions. Since our problem is a ledge on a wide glacial bed, we will continue with plane strain but note when a quantity would differ for plane stress.

2.2   Linear Elastic Fracture Mechanics (LEFM)

While it may seem counterintuitive to approach fracture – which involves permanent (i.e. plastic) deformation in the form of crack growth – from the standpoint of linear elasticity, the approach has a number of advantages, not least including the use of a fairly simple and well-studied material model for our calculations. In many solids, and especially in rocks, during most fracture processes we can assume that nearly all of the solid undergoes infinitesimal elastic strain, except in the immediate vicinity of the crack tip. This assumption is called small-scale yielding [5], and it allows us to avoid directly including the complex multiscale process of fracture extension in our model. Instead, we calculate fracture mechanical parameters from our linear elastic solution, which allow us to then make predictions about fracture paths and propagation rates.

The most important fracture mechanical parameters are called stress-intensity factors (SIFs), for which straightforward models have been developed to relate the SIFs to fracture behavior. The stress intensity factors indicate the magnitude of the stress singularity around the crack tip, and are widely used to predict and assess crack behavior in experimental, theoretical, and numerical studies of fracture.

2.2.1   Modes of Fracture

Stress fields in linear elastic solids exhibit a superposition principle similar to waves, where if a complex problem can be reduced to a simpler set of loading conditions where the solutions are known, then the complex solution to the stress field is simply a linear combination of the simpler forms [6, pp. 85-6]. In the case of fracture, this allows for the identification of a set of fundamental loading conditions (or "modes" of fracture), from which any situation

can be derived. These are opening mode (mode-I), in-plane shearing mode or sliding mode (mode-II), and out-of-plane shearing mode (mode-III) (Figure 2.3) [5]. In the case of a two dimensional problem, we limit ourselves to modes I and II, since mode-III fracture would propagate out of our model domain.

(a) Mode I
opening

(b) Mode II
shearing
(in-plane shear)

(c) Mode III
tearing
(out-of-plane shear)
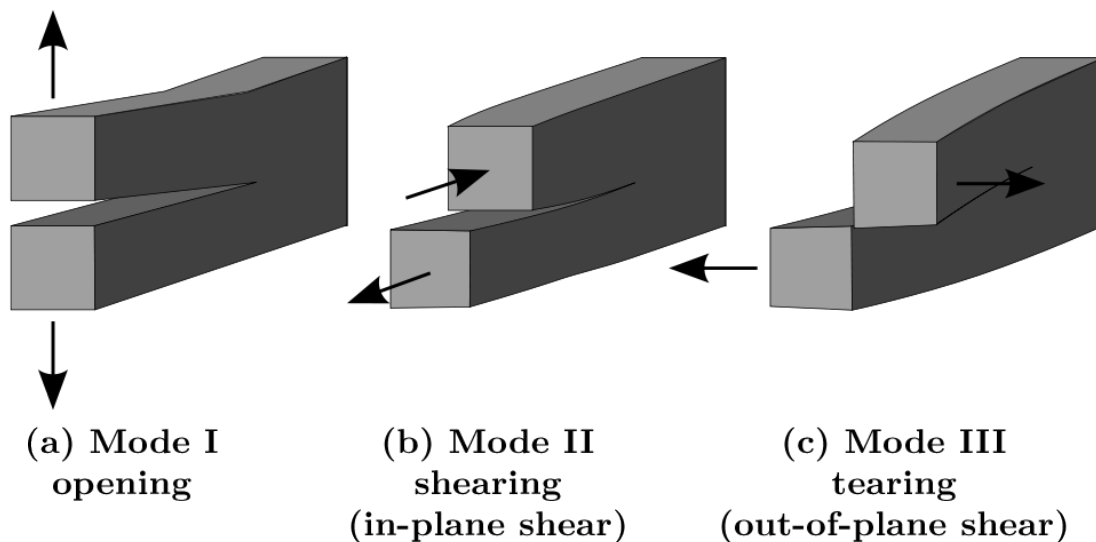
Figure 2.3: three fundamental modes of fracture. In 2D, only the first two modes are used. [2]

Typically, fracture mechanics problems begin by identifying the fracturing mode, which is determined by the orientation of the boundary tractions on the solid (ie loading conditions). Each fracturing mode has its own stress-intensity factor, called K_I, K_{II}, and K_{III}, respectively. Mode-I fracture is the most widely studied, with analytic solutions relating the mode-I SIF to the loading stress and crack length for a range of geometries and loading conditions, which generally takes the form of

$$K_I = Y\sigma\sqrt{\pi a}, \tag{2.9}$$

where a is the crack length, σ is the far-field tensile stress, and Y is a correction factor which depends on the specimen geometry [5]. Equation (2.9) is an elegant result applicable

---

[2]Figure adapted from https://commons.wikimedia.org/wiki/File:Fracture_modes_v2.svg

to a wide range of mode-I problems, but for our study we need numerical methods to solve for general mixed-mode fracture.

2.2.2 Fracture Propagation Direction

Mode-I fractures propagate in a straight-line path, whereas our other modes and mixed-mode problems tend to propagate at an angle from the initial fracture orientation [5]. This phenomenon makes sense in light of the stresses actually required for fracture propagation – in order for the crack to extend, stresses must exist at the crack tip to pull the crack faces apart, where mode-I loading conditions apply this greatest tensile stress along the direction of initial fracture. Extending this reasoning to fracture generally, we can predict propagation path in the direction of the greatest tensile stress at the crack tip, which is formalized at the Maximum Tangential Stress (MTS) criterion for fracture propagation [7].

Fortunately, for an isotropic elastic solid, the displacement field around the crack tip is known exactly for a given combination of K_I and K_{II}. The first-order x-displacement u and the y-displacement v in polar coordinates around the crack tip (which are exact as $r \to 0$) are given as [8]

$$u_I = \frac{K_I}{4\mu} \sqrt{\frac{r}{2\pi}} \left[(2\kappa - 1) \cos\left(\frac{\theta}{2}\right) - \cos\left(\frac{3\theta}{2}\right) \right] \tag{2.10}$$

$$u_{II} = \frac{K_{II}}{4\mu} \sqrt{\frac{r}{2\pi}} \left[(2\kappa + 3) \sin\left(\frac{\theta}{2}\right) - \sin\left(\frac{3\theta}{2}\right) \right] \tag{2.11}$$

$$v_I = \frac{K_I}{4\mu} \sqrt{\frac{r}{2\pi}} \left[(2\kappa + 1) \sin\left(\frac{\theta}{2}\right) - \sin\left(\frac{3\theta}{2}\right) \right] \tag{2.12}$$

$$v_{II} = -\frac{K_{II}}{4\mu} \sqrt{\frac{r}{2\pi}} \left[(2\kappa - 3) \cos\left(\frac{\theta}{2}\right) - \cos\left(\frac{3\theta}{2}\right) \right] \tag{2.13}$$

$$u = u_I + u_{II} + \mathcal{O}(r^2), \qquad v = v_I + v_{II} + \mathcal{O}(r^2), \tag{2.14}$$

where subscripts I and II designate our mode-I and mode-II components respectively, κ is a material parameter equal to $3 - 4\nu$ for plane strain where ν is Poisson's ratio, and μ is the shear modulus.

The tensile stress in a given direction is described by the $\sigma_{\theta\theta}$ component of the stress tensor in polar coordinates, so we must convert equation (2.14) from displacement to

9

strain (eq. (2.4)), strain to stress (eq. (2.7)), and cartesian to polar coordinates. After these transformations, we obtain

$$\sigma_{\theta\theta} = \frac{1}{\sqrt{2\pi r}} \cos\frac{\theta}{2} \left[\frac{K_I}{2}(1 + \cos\theta) - \frac{3K_{II}}{2}\sin\theta \right]. \tag{2.15}$$

The direction of maximum tensile stress, θ_c, occurs when $\sigma_{\theta\theta}$ is maximized, meaning

$$\left.\frac{\partial\sigma_{\theta\theta}}{\partial\theta}\right|_{\theta=\theta_c} = 0, \quad \left.\frac{\partial^2\sigma_{\theta\theta}}{\partial\theta^2}\right|_{\theta=\theta_c} < 0. \tag{2.16}$$

Neglecting r dependence, this evaluates to

$$K_I \sin\theta_c - K_{II}(3\cos\theta_c - 1) = 0, \tag{2.17}$$

$$K_I \cos\frac{\theta_c}{2}(1 - \cos\theta_c) + K_{II}\sin\frac{\theta_c}{2}(9\cos\theta_c + 5) < 0. \tag{2.18}$$

The roots of (2.17) are

$$\theta_c = 2\tan^{-1}\left(\frac{1}{4}\left(\frac{K_I}{K_{II}} \pm \sqrt{\left(\frac{K_I}{K_{II}}\right)^2 + 8} \right) \right). \tag{2.19}$$

Equation (2.19) has been shown to agree well with observations, with $\theta_c = 0$ for pure mode-I, and $\theta_c = 70.5°$ for pure mode-II. Thus, in two dimensions, predictions can be made for the crack propagation path under arbitrary loading conditions once K_I and K_{II} are known. Dynamically, the MTS criterion tells us that as mixed-mode fractures propagate, mode-I comes to predominate over the course of propagation. Evaluation techniques for our mixed-mode stress-intensity factors will be discussed in the numerical methods section of our study (section 3.2).

If we have slow, subcritical growth, then we treat propagation as a succession of static equilibrium states, where we can propagate the crack forwards outside the model, without an explicit time dependence.

It is worth noting that the maximum tangential stress criterion is the most popular in use, due to its simplicity and its reliability, but other criteria have also been proposed, with varying degrees of complexity [5]. For the purposes of our study, we will only be using the MTS criterion.

2.2.3 Fracture Propagation Rates

Fracture propagation is generally grouped into the categories of stationary (no propagation), subcritical (stable propagation), and critical (unstable propagation or failure). Since the defining study on the topic [9], the approach is usually applied as follows:

$$V_c = \begin{cases} 0, & K_I < 0.3K_{Ic}, \\ A(K_I)^m, & 0.3K_{Ic} < K_I < K_{Ic}, \\ V_s \approx \sqrt{E/\rho}, & K_I > K_{Ic}, \end{cases} \tag{2.20}$$

where V_c is our crack propagation velocity, K_{Ic} is a material parameter called the mode-I critical fracture toughness, E is the Young's Modulus of the material, ρ is the density of the material, and A and m are empirical parameters which are generally less well constrained than E or K_{Ic}. Our ranges correspond to a stationary crack ($K_I < 0.3K_{Ic}$), a subcritically propagating crack ($K_I < K_{Ic}$), and a critically propagating crack ($K_I > K_{Ic}$). The form of equation (2.20) is a simple expression called "Charles' Law" used to approximate experimental results for subcritical crack growth, and describes a highly nonlinear relationship between K_I and V_s, often with $m = 50$ or greater [10].

The subcritical growth threshold of $0.3K_{Ic}$ is also a rough estimate proposed by [9], with some uncertainty but little experimental data on the precise threshold, due to the difficulty of creating small SIFs in the lab. Subcritical propagation in rocks is roughly on the order of a few millimeters to centimeters per day, whereas critical fracture often travels at hundreds of meters per second, which is effectively instantaneous for our purposes.

The reader will note that equation (2.20) expresses V_c only as a function of K_I, which indicates the extent to which mode-II fracture velocity research is emerging only recently, and this author has not been able to find any research in the literature on subcritical rock fracture velocities for mixed-mode loading. For mode-II, some researchers have evaluated K_{IIc} as a separate material parameter from K_{Ic} [11],[12],[13] and have calculated Charles' law parameters for pure mode-II loading ($V_{c_2} = A_2(K_{II})^{m_2}$) [10]. Some numerical fracture studies in other materials [14] assume $V_c(K_I, K_{II}) = V_{c_1}(K_I) + V_{c_2}(K_{II})$, but to date no rock experiments have been carried out to verify this assumption. While mixed-mode subcritical fracture research is basically non-existent, more robust research exists for determining the critical failure threshold in engineering materials (e.g. concrete instead of rock) for mixed-

mode conditions [7]. Structural engineers will often use the simple threshold of

$$K_{norm} = \sqrt{K_I^2 + K_{II}^2} < K_{Ic},$$
(2.21)

which is noted to be somewhat conservative compared to other more complex criteria [7].

Due to the limitations of the linear elastic macroscopic paradigm, this author predicts that future studies of subcritical crack growth rates will be directed towards paradigms which encompass more of the microphysical basis for rock fracture. For the purposes of our study, we will simply assume that mode-I growth rates place a lower limit on mixed-mode results.

Chapter 3

Methods

In our fracture mechanics simulations, our main objective is to solve for the stress-intensity factors of our crack. In order to do this, we must first solve for the stress state inside our solid. We detail the governing equation for our isotropic linear elastic material, which we solve using a modified form of the finite element method specifically developed for fracture. We can then evaluate the stress-intensity factors via post-processing of our solutions, from which we can draw conclusions about fracture propagation directions and rates.

3.1 Finite Element Method

3.1.1 Governing Equation

In order to solve for the equilibrium stress state in our solid, we rewrite Newton's second law [3, pp. 117-8] in N/m^3 as

$$\vec{\nabla}\boldsymbol{\sigma} + \rho\vec{F} = \rho\frac{\partial^2\vec{u}}{\partial t^2}, \tag{3.1}$$

where $\vec{F}$ are body forces which are distributed throughout our solid, such as gravity. We solve for stress equilibrium, so $\frac{\partial^2\vec{u}}{\partial t^2} = 0$, and we also do not consider body forces in our model. Substituting our displacement-strain relation (eq. (2.4)) and our stress-strain relation (eq. (2.7)) into our equation of motion (eq. (3.1)), we obtain

$$(\lambda + \mu)\vec{\nabla}(\vec{\nabla}\cdot\vec{u}) + \mu\nabla^2\vec{u} + \rho\vec{F} = \rho\frac{\partial^2\vec{u}}{\partial t^2}, \tag{3.2}$$

13

which gives us one coupled second-order partial differential equation for each of our spatial components, with the displacement as our sole field variable to solve. This system of PDEs, called the vector Laplace equation, is elliptic as long as $\lambda/\mu > -2$, which is true by the definition of λ and μ for solids. This means that we can expect a solution for equation (3.2) once we set conditions for either $\vec{u}$ or $\nabla \vec{u}$ on all boundaries of our domain. For our study, we use the finite element method (FEM) as our numerical technique to solve equation (3.2).

3.1.2 Finite Element Method for Solid Mechanics

The standard finite element method involves a discretization of our solution domain into a geometrically contiguous mesh of simplices (figure (3.1)), which are line segments in one dimension, triangles in two dimensions, and tetrahedra in three dimensions. Each simplex is called an element, and the corners of an element are called nodes. The solution to our field variable $\boldsymbol{u}$ [1] is calculated on each node, but when evaluating our field variable outside the nodal points, some smooth interpolation must be done. This is accomplished in one dimension, for example, using the Lagrange interpolating polynomials. For our simplified presentation of FE, we describe the solution space between nodes with linear interpolation functions ϕ_i.[2] Each node, positioned at $\boldsymbol{x}_i$, has a corresponding interpolation function ϕ_i. Each interpolation function is defined equal to 1 on its node, and 0 on all other nodes. This can be stated as

$$\phi_i(\boldsymbol{x}_j) = \begin{cases} 1 & i = j \\ 0 & i \neq j \end{cases}. \tag{3.3}$$

FEM solves for the value of our field variable $\boldsymbol{u}$ at each node i, which we call $\boldsymbol{u}_i$. Using our interpolation functions, an arbitrary point $\boldsymbol{x}$ in our solution domain is thus

$$\boldsymbol{u}(\boldsymbol{x}) = \sum_i \boldsymbol{u}_i \phi_i(\boldsymbol{x}). \tag{3.4}$$

---

[1]Whereas we previously reserved $\boldsymbol{x}$ for tensors and $\vec{x}$ for vectors, we use $\boldsymbol{x}$ to mean a vector until we begin referring to tensors again in section 3.2.

[2]Elements with linear interpolation functions are called first-order elements, and elements with additional polynomial interpolation functions are called higher-order elements.

Each coefficient $\boldsymbol{u}_i$ is called a degree of freedom (DOF) of our solution. One important property of our interpolation functions ϕ_i is that they obey partition of unity, meaning

$$\sum_i \phi_i(\boldsymbol{x}) = 1 \tag{3.5}$$

for all $\boldsymbol{x}$. If this property was not satisfied, our solution could not resolve a constant value for $\boldsymbol{u}$ and thus would be sensitive to translations of our domain or alterations of our mesh.

Note that we have just described the most basic form of FEM with first-order Lagrangian elements, where additional features include the use of special interpolation functions [15], the definition of additional nodes inside each element, meshing with non-triangular elements [16], etc. For our study, we use a modified form of FEM which adds fracture-specific basis functions to the solution space in order to improve accuracy.
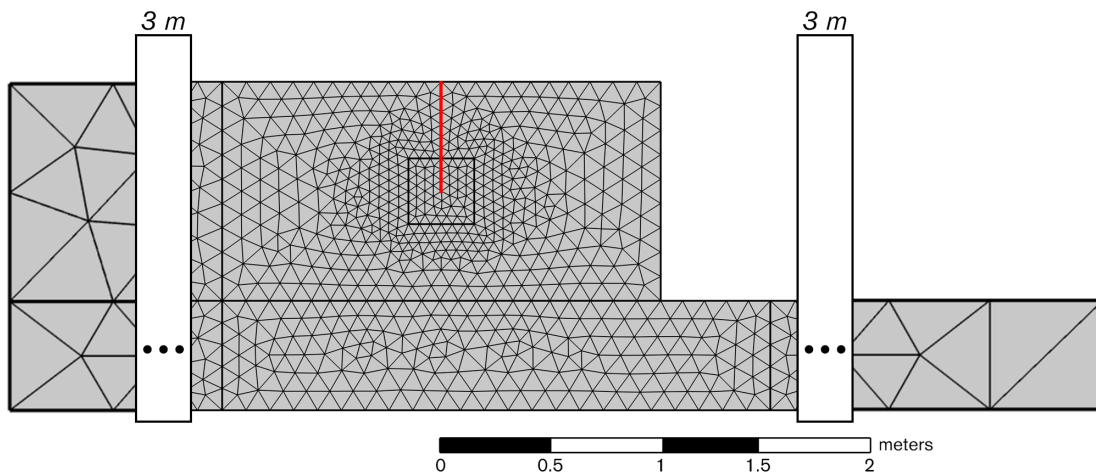

Figure 3.1: Example free triangular mesh used for our quarrying problem. Each triangle is an element, and each vertex is a node. Fracture location indicated by red line, with the finest mesh located around the crack tip, growing coarse by the ends of our model domain. Ellipses indicate 3 meter regions of our domain which are omitted to preserve display clarity around the crack tip.

3.1.3 Extended FEM for Fracture Mechanics

The standard finite element described in the previous section has difficulties solving for the displacement field around crack tips, owing to the discontinuous and nonlinear solutions which are expected analytically (eqs (2.10–2.13)); a typical solution is shown in the lower row of figure (3.2). Since these patterns are ultimately dependent on θ rather than r, some element will always contain a discontinuity, and thus mesh refinement has a limited effect on improving the likelihood of converging on a solution.

Today, the most popular method of dealing with this problem is a modification to standard FEM proposed by [17], which they named the eXtended Finite Element Method (XFEM). It involves the addition of special functions to the DOFs of crack-adjacent or crack-containing elements to better enable the solver to reproduce the discontinuous behavior expected from the analytic solution for near-tip displacements (equation (2.14)). These special basis enrichment functions fall into two types: (1) near-tip asymptotic function enrichment to handle the crack-tip discontinuity, and (2) Heaviside or jump function enrichment to include fractures directly in the displacement field solutions to avoid remeshing.

3.1.3.1 Asymptotic Enrichment

To handle the crack-tip displacement field, we introduce four functions $F_L(r, \theta)$ defined in a polar coordinate system with the crack tip at the origin (figure (3.3)). Our four asymptotic functions are

$$F_1 = \sqrt{r} \sin \frac{\theta}{2} \tag{3.6}$$

$$F_2 = \sqrt{r} \cos \frac{\theta}{2} \tag{3.7}$$

$$F_3 = \sqrt{r} \sin \frac{\theta}{2} \sin \theta \tag{3.8}$$

$$F_4 = \sqrt{r} \cos \frac{\theta}{2} \sin \theta, \tag{3.9}$$

which are plotted in the top row of figure (3.2) – note that only F_1 is discontinuous where we define $\theta \in [-\pi, \pi]$. With some trigonometry, it can be shown that the set $\{F_L\}$ spans the expected analytic solution space (eqs (2.10–2.13)), but it is visually plausible from figure (3.2) alone that F_L could reproduce the necessary behavior for our example solution.
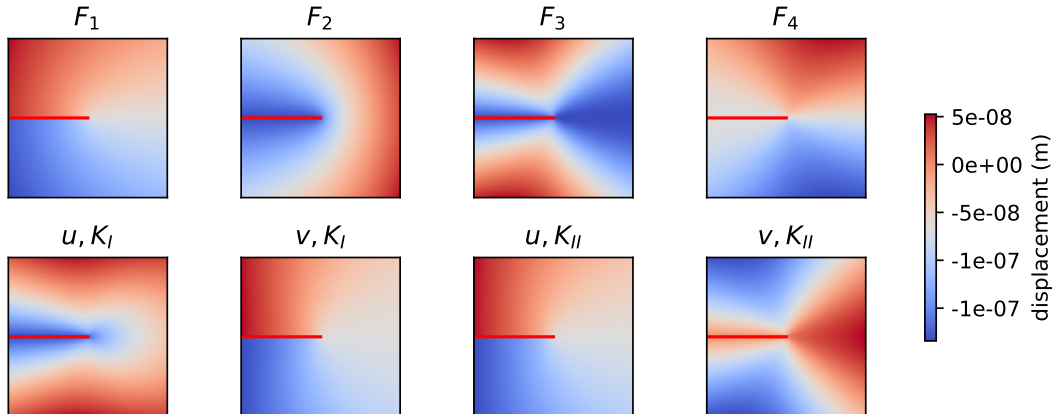
16

Figure 3.2: Near-crack displacement fields for our basis enrichment functions F_l (equations (3.6–3.9)) plotted above analytic displacement fields (equations (2.10–2.13)) evaluated for our model parameters (see table) and $K_{I,II} = 1 \times 10^6$ MPa/$\sqrt{\text{m}}$ for comparison. Note that the discontinuity in v_{II} and u_I arise from θ rather than r dependence, making our sharp gradients and discontinuities size-independent.

We add these basis functions to any node which contains the crack tip in the interior of one of its elements, depicted by the crossed boxes in figure (3.4). In these nodes, our modified basis is

$$\boldsymbol{u}(\boldsymbol{x}) = \sum_i \boldsymbol{u}_i \phi_i + \sum_i \sum_{L=1}^{4} \boldsymbol{a}_{iL} F_L \phi_i, \tag{3.10}$$

where we our interpolation functions preserve partition of unity (eq (3.5)) in the crack-tip containing element, but fail in elements which contain non-enriched nodes. This is one weakness of the initial presentation of XFEM [17], which has been addressed via the addition of blending functions in certain implementations [7]. Additionally, authors vary in the extent around the crack tip which gets enrichment of the form of equation (3.10) [18].

3.1.3.2 Step Function Enrichment

In traditional FEM, fractures much be prescribed as a void within the model geometry, which requires meshing to the crack boundary of a predetermined shape and width. During crack growth simulations, the solid must then be remeshed for each solution step, where remeshing can be a computationally expensive task. In XFEM, cracks are included in the displacement field solution instead of the model geometry, which makes fracture placement independent of the mesh and eliminates the need for remeshing (figure (3.4)).

In XFEM, cracks are described as sharp discontinuities in the displacement field within the elements along the fracture location (circled nodes in figure (3.4)), where the fracture discontinuity enrichment function is [17]

$$H(x) = \begin{cases} 1 & x \geq 0 \\ -1 & x < 0 \end{cases}. \tag{3.11}$$

In order to to specify the orientation of our jump, and thus our fracture, we introduce a function $f(\boldsymbol{x})$ which is negative when $\boldsymbol{x}$ is below the crack, and positive when $\boldsymbol{x}$ is above. In the XFEM literature, $f(\boldsymbol{x})$ is called a level-set function. If we have a straight-line crack oriented along the x-axis, we simply have $f(\boldsymbol{x}) = \boldsymbol{x} \cdot \hat{\boldsymbol{y}}$. For an arbitrarily curved crack Γ_c, we instead have

$$f(\boldsymbol{x}) = \min_{\bar{\boldsymbol{x}} \in \Gamma_c} \|\boldsymbol{x} - \bar{\boldsymbol{x}}\| \cdot \text{sign}(\boldsymbol{n}^+ \cdot (\boldsymbol{x} - \bar{\boldsymbol{x}})), \tag{3.12}$$

where $\bar{\boldsymbol{x}}$ is the closest point on Γ_c to $\boldsymbol{x}$, and $\boldsymbol{n}^+$ is a vector normal to Γ_c at $\bar{\boldsymbol{x}}$. In these nodes, our basis is

$$\boldsymbol{u}(\boldsymbol{x}) = \sum_i \boldsymbol{u}_i \phi_i + \sum_i \boldsymbol{b}_i H(f(\boldsymbol{x})) \phi_i. \tag{3.13}$$

Together equation (3.13) describes the body of our crack, and F_1 (figure (3.2)) terminates it. We can thus represent the basis in our entire solid as

$$\boldsymbol{u}(\boldsymbol{x}) = \sum_i \boldsymbol{u}_i \phi_i + \sum_{i \in \Omega_F} \sum_{L=1}^{4} \boldsymbol{a}_{iL} F_L \phi_i + \sum_{i \in \Omega_H} \boldsymbol{b}_i H(f(\boldsymbol{x})) \phi_i, \tag{3.14}$$

where Ω_H is the region of step-function enrichment, and Ω_F is the area of crack-tip enrichment, represented by the circled and boxed nodes of figure (3.4), respectively. Our

additional degrees of freedom are $\boldsymbol{a}_{iL}$ and $\boldsymbol{b}_i$, which have no physical meaning compared to our standard DOFs $\boldsymbol{u}_i$.

Due to its continuity with standard FEM, this scheme for fracture representation has been adopted by most major structural analysis packages (ANSYS, ABAQUS, COMSOL), and has become the most popular method of fracture representation in the field of numerical fracture mechanics [19].
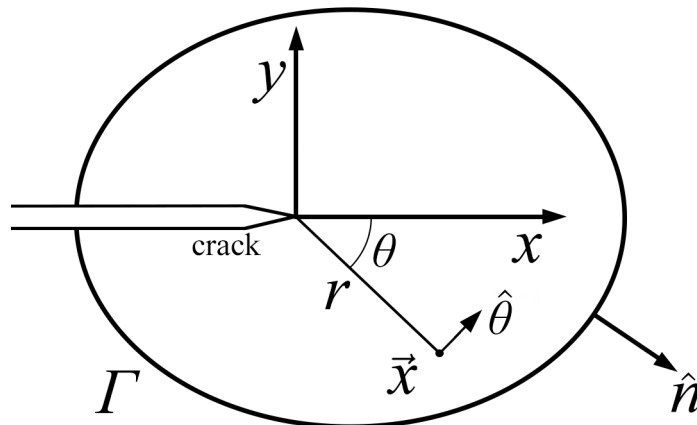

Figure 3.3: Definition of crack-tip local coordinate frame, where x is called the crack-tip extension vector, and Γ is an example crack-tip integration contour for our J-integral (section 3.2).

3.2 Stress-Intensity Factor Evaluation

Once we have obtained numerical solutions for the displacement field in our solid, we need some means to evaluate the stress-intensity factors of our crack. While we could directly extrapolate K_I, K_{II} from our near-tip displacements [8], our solution is more accurate outside the near-tip region, especially when not using crack-tip enrichment. In the late 1960s, Rice [20] and Cherapanov [21] independently discovered a path-independent integral which is directly related to K_I, thus allowing for SIF evaluation based on our tip-distal solutions for stress and displacement. Rice named this quantity the J-integral, which has
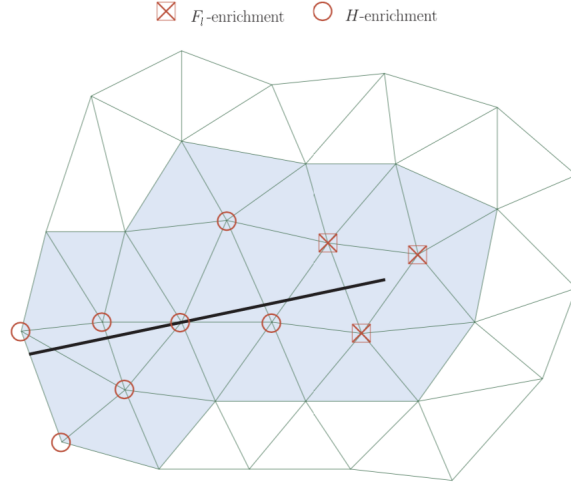
Figure 3.4: Example node enrichment scheme. Figure reprinted from [18].

a number of uses in fracture mechanics.[3]

The classical J-integral is given as

$$J_1 = \int_\Gamma \left(W\hat{n} \cdot \hat{x} - \vec{T} \cdot \frac{\partial \vec{u}}{\partial x} \right) ds, \tag{3.15}$$

where

W = the strain energy density, defined as $\frac{1}{2}(\boldsymbol{\sigma} : \boldsymbol{\varepsilon}) = \frac{1}{2}(\sigma_{xx}\varepsilon_{xx} + 2\sigma_{xy}\varepsilon_{xy} + \sigma_{yy}\varepsilon_{yy})$,

Γ = contour around the crack-tip,

$\hat{n}$ = outward unit normal vector to Γ,

$\vec{T}$ = traction along Γ in the $\hat{n}$ direction (defined as $\vec{T} = \boldsymbol{\sigma}\hat{n}$),

$\vec{u}$ = displacement,

$\hat{x}$ = crack-tip extension vector,

ds = path element along Γ.

A typical integration curve with labeled quantities is shown in figure (3.3). For pure mode-I loading, we simply have

$$K_I = \sqrt{J_1 E^*}, \tag{3.16}$$

---

[3]Griffiths showed that the J-integral can be understood as the strain-energy release rate – i.e. the energy released per unit length of crack growth, which is used widely in the energy balance (thermodynamic) analysis of cracks [7].

20

where E^* is the effective Young's Modulus, defined as

$$E^* = \begin{cases} E, & \text{plane stress,} \\ \dfrac{E}{1-\nu^2}, & \text{plane strain,} \end{cases} \tag{3.17}$$

where ν is Poisson's ratio. In general, however, J_1 depends on both K_I and K_{II}. In order to obtain both stress intensity factors, we need an another quantity. In 1975, Hellen [22] introduced a new path integral J_2 which is defined as

$$J_2 = \int_{\Gamma} \left(W \hat{n} \cdot \hat{y} - \vec{T} \cdot \frac{\partial \vec{u}}{\partial y} \right) ds, \tag{3.18}$$

where we have exchanged the crack-tip extension direction x for the crack-tip normal direction y, but all other variables remain the same. The relations between J_1, J_2 and mode-I and mode-II stress intensity factors K_I, K_{II} are

$$J_1 = \frac{K_I^2 + K_{II}^2}{E^*}, \qquad J_2 = \frac{-2 K_I K_{II}}{E^*}; \tag{3.19}$$

$$K_I = \frac{1}{2}\sqrt{E^*(J_1 - J_2)} + \sqrt{E^*(J_1 + J_2)}, \qquad K_{II} = \frac{1}{2}\sqrt{E^*(J_1 - J_2)} - \sqrt{E^*(J_1 + J_2)}. \tag{3.20}$$

Note that equation (3.20) reduces to (3.16) when $K_{II} = 0$. Studies have shown that the evaluation of J_2 in path integral form (eq. (3.18)) yields less reliable results than calculating J_1 using equation (3.15). Most researchers improve this situation by converting these into domain integrals, or by devising other evaluation techniques (cit. IIM, ASD, DEM). In this study, we use COMSOL5.6's built-in SIF evaluation technique, which avoids direct evaluation of J_2 by estimating the mode mixing ratio $\beta = K_I/K_{II}$ from the near-tip displacements. Equation (3.19) can then be rearranged to give K_I and K_{II} from J_1 and β.

Chapter 4

Experiment

In this study, we conduct mixed-mode fracture simulations to investigate some basic assumptions of the existing literature on quarrying. After a brief discussion of this literature and the problem, we describe our results, which show that the fracture mechanics used in existing quarrying literature has a number of shortcomings.

4.1   Quarrying Problem

In 1996, Hallet proposed an idealized 2D model [2] to study quarrying in a stepped bed. This simplified bed geometry is believed to create the conditions which most strongly favor quarrying, thus providing a framework from which researchers can draw basic theoretical insights about this process.

   For quarrying to occur, two conditions must be satisfied: (1) bed obstacles must be shaped so that propagating fractures can actually isolate bedrock blocks, and (2) boundary tractions must induce strong deviatoric, rather than hydrostatic,[1] compressive stresses in order to cause fracture propagation.

   Underneath a glacier, we have purely compressive loading due to the weight of the ice and flowing meltwater. The weight of the ice applies a uniaxial normal load (σ_I) to our rock, while a layer of pressurized meltwater makes any shear traction due to drag negligible

---

[1]Hydrostatic stress is applied equally to the boundaries of a volume, and is given as $\sigma_H = \text{tr}(\boldsymbol{\sigma})/2$ for 2D. Deviatoric stress is simply $\boldsymbol{\sigma} - \sigma_H \boldsymbol{I}$, which can have both normal and shear components.
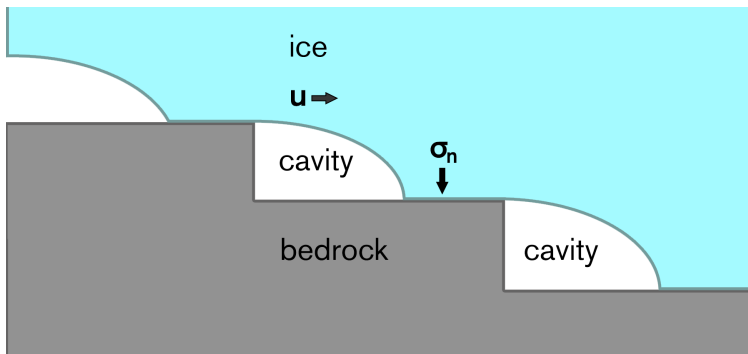
Figure 4.1: Idealized stepped bed geometry, believed to provide the most favorable conditions for quarrying. Ice moving at horizontal velocity u with a normal stress σ_n applied in the area of ice-bed contact. This bed shape is relatively uncommon with glaciers, but it has been observed in the field (see figure (1.1)).

for our purposes. Additionally, the meltwater applies a uniform hydrostatic compressive stress σ_W, which actually drives crack closure (hydrostatic compression would squeeze cracks shut). Our loading is thus an effective pressure [2],[23],[24] given by

$$\sigma_n = \sigma_I - \sigma_W. \tag{4.1}$$

As ice slides past a ledge, it takes a certain amount of time for the ice to sag downwards. Since the glacier is moving at a certain velocity, this ice creep creates cavities which concentrate the weight of the glacier on a fraction of the step. This deviatoric stress then drives quarrying on ledge corners.

In his analysis of the problem, Hallet uses an analytic solution for the boundary stresses induced by the loading in figure (4.1). The situation corresponds to a quarter-plane (i.e. a plane bounded on two sides) with a uniformly distributed normal load. The solution shows an induced tensile stress $2\sigma_n/3$ in the area just up-glacier of ice-bed contact, where Hallet assumes a fracture will be initiated, since crack propagation is driven by tensile stress (section 2.2.2). Unfortunately, Hallet assumes that this tensile stress creates mode-I fracture, but by comparison to figure (2.3), we can see that this loading situation more resembles mode-II fracture. Hallet then assumes that the stress state inside the step corresponds to a crack under a uniform tensile load (mode-I), which allows him to use the standard result of equation (2.9), with a tensile stress of $2\sigma_n/3$ and a geometry correction

factor Y of $2/\pi$. This gives

$$K_I = \frac{2}{\pi} \frac{2\sigma_n}{3} \sqrt{\pi a}, \tag{4.2}$$

where a is our crack length. He then parameterizes the quarrying rate according to the ledge proportions, ice velocity, and the ice-bed contact area. Previous work [1] has shown that (4.2) corresponds poorly to the numerical results for K_I as a function of a for mode-I fracture, demonstrating that the internal stress state in the step cannot be neglected. In this study we show that this fracture problem presented by Hallet is a fundamentally mixed-mode problem, requiring numerical modeling to predict both crack growth direction and growth rates.

4.2 Model Design
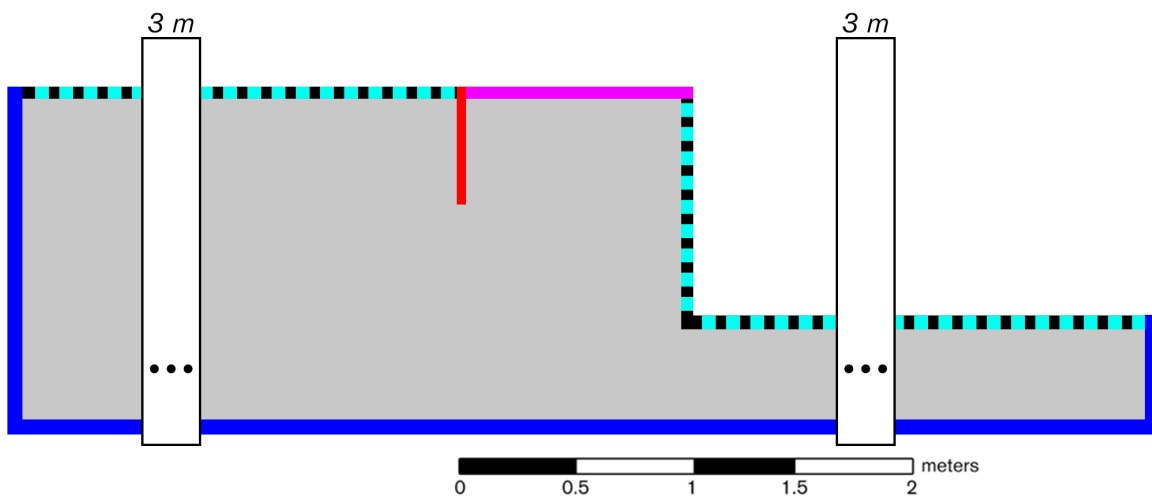
Figure 4.2: Model domain with coloration to indicate fracture location and boundary conditions. Free boundaries are dashed cyan, normal load is the purple line at the step ledge, displacement is set to zero on the outer blue lines, and our fracture location is indicated by the vertical red line. Vertical boxes with ellipses indicate 3 meter regions of our step removed for figure readability.

For our experiment, we use all the methods described above in the FEM package COMSOL to conduct mixed-mode simulations of fracture for Hallet's quarrying model.

We model a single step ledge 1 meter in height, with a distributed normal load of 2 MPa applied to 1 meter of our ledge, treating the rest of the outer surfaces of the ledge as a free boundary, as shown in figure (4.2). We then extend our ledge for 5 meters on both sides of our loading region in order to avoid artificially imposed boundary effects. We include 1.5 meters of solid below the loaded portion, after which we set our displacement to zero on the lower and outer boundaries, which represents the extent after which the displacements in our rock mass effectively go to zero. After Hallet, we place a fracture at the edge of ice-bed contact. We use a free triangular mesh for our solid, with small elements around our fracture which grow to large elements in the outer portions of our step, as shown in figure (3.1).

We use the extended finite element method to solve for infinitesimal strains in a linear elastic material with a single edge crack (sections 3.1 and 3.1.3), using material parameters for Westerley granite (see table). We evaluate the J-integral around our crack and estimate the mode-mixing ratio β from our crack-tip displacement, from which we can infer our stress intensity factors K_I and K_{II} (section 3.2). We then evaluate the maximum tangential stress criterion from our stress intensity factors in order to determine fracture propagation direction (section 2.2.2).

Chapter 5

Results

Our model predicts that fractures curves towards the step ledge, which is in agreement with the limited experimental data, and that the total magnitude of our SIFs is greater than previously assumed.

5.1   Influence of fracture orientation on propagation

A previous study of the same problem [1] showed that the mode-I SIF for bed-normal fracture actually decreases with crack length, rather than the $\sqrt{a}$ increase predicted in equation (4.2). Our rotation angle, along with a typical solution for the stress field, is shown in figure (5.1), which shows a concentration of stress near the step ledge. Since the MTS criterion tells us that fractures propagate towards concentrations of stress, we examine the effect of angling our fractures.

Keeping the fracture at the edge of ice-bed contact, we calculate K_I and K_{II} for a range of fracture lengths a and angles θ for a straight-line crack. Note that our simulations are not dynamical – we simply calculate the SIFs for a pre-defined crack length and orientation. The results are shown in figure (5.2), where we have plotted the existing prediction by Hallet as a dashed line.

Our results show that for a bed-normal crack ($\theta = 0$), mode-II fracture dominates over mode-I, whereas previous literature has assumed the mode-II component to be negligible. This confirms our hypothesis of curved cracks, since mode-II fractures propagate at about
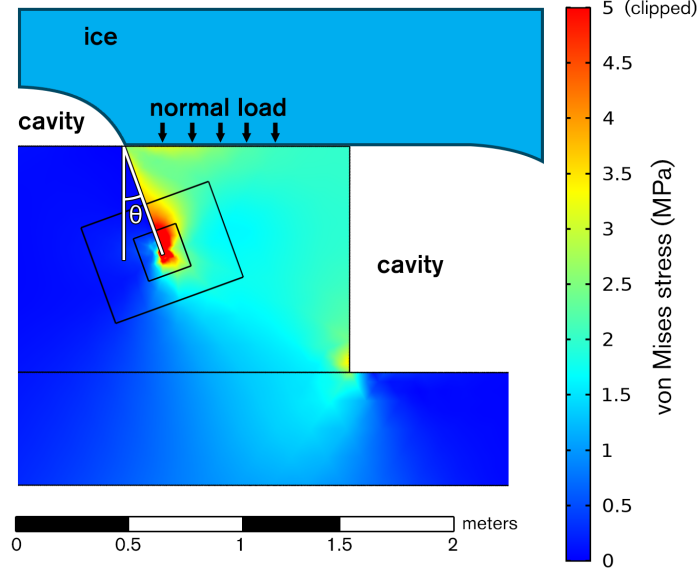
Figure 5.1: Typical solution for the stress field for a rotated straight-line crack. The white, tilted right line is our fracture with length $a = 0.5$ m and tilt $\theta = 30°$.

a 70° angle (section 2.2.2). This poses a problem for assessing crack growth, however, since no literature exists on the mode-II or mixed-mode subcritical growth threshold in rocks.

For our angled fractures, which we expect to be more realistic, we see exponential crack growth, as well as an order of magnitude increase in the mode-I SIF for $\theta = 30°$ compared to $\theta = 0$. This suggests a greater likelihood of critical failure as our fracture propagates through the step, which is conservatively estimated to occur when $(K_I^2 + K_{II}^2)^{1/2} > K_{Ic}$ (equation (2.21)), which we also plot below. Due to this dramatic dependence of K_I and K_{II} on the orientation of our fracture, we must numerically evaluate the propagation angle instead of simply stipulating it in our model.

5.2   Pseudo-vector field for crack propagation

In order to assess whether highly angled cracks are physically likely, we evaluate the Maximum Tangential Stress (MTS) criterion for propagation direction over an ensemble of straight-line fractures. The MTS criterion, equation (2.19), gives us a physical propaga-
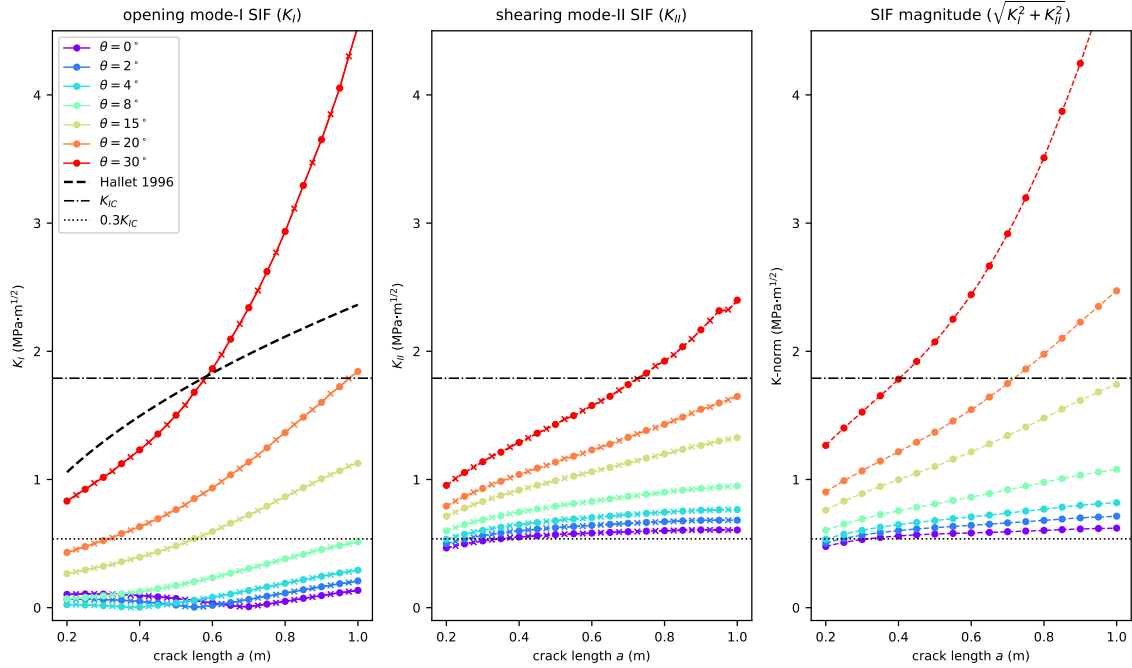
Figure 5.2: Stress intensity factors for rotated straight-line cracks. Results shown for cracks centered at the edge of 2 MPa ice-loading, evaluated for two contours, indicated by 'o' and 'x' markers. We also plot K_{norm} (eq. (2.21)) to see the mixed-mode failure threshold, which is estimated to occur when $K_{norm} > K_{Ic}$ (dot-dashed line).

tion angle θ_c in terms of K_I and K_{II}, which we obtain as described above. Since we are unable to simulate arbitrary crack propagation in our model, we evaluate the physical propagation angle θ_c for a range of straight-line fractures which begin at the edge of ice-bed contact and terminate at different points throughout our step. We plot our results in figure (5.3) below, where each arrow represents the MTS criterion evaluated for one simulation of a straight-line crack beginning at the origin and terminating at the arrow base.

Our results show a near-uniform angling of cracks towards the step ledge, with $\theta_c \approx 70°$ for our strongly mode-II fractures along $x = 0$. This suggests that, for an isotropic linear elastic material with uniform strength, bed-normal propagation is highly unlikely, which means that we predict less quarried mass per step than the standard assumption of rectangular quarried masses. This curving trend is so strong that as our fractures approach the step ledge, they propagate bed-parallel, even curving upwards just at the edge of the
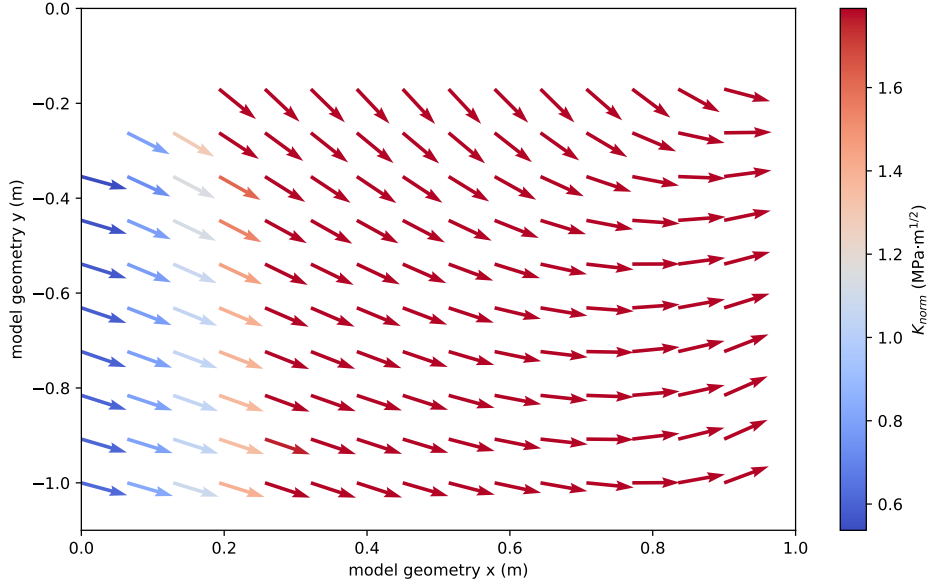
Figure 5.3: Propagation direction evaluated for straight-line cracks centered at the origin. Arrows are colored by K_{norm}, with the scale clipped at the critical fracture toughness. Our plot area has the loading surface along $0 < x < 1, y = 0$, and our unloaded step edge along $-1 < y < 0, x = 1$, where our evaluation method prohibits us from examining fractures with $x > -0.2$.

step.

This upward curve, however, seems physically unlikely, and may arise due to the fact that our J-integral contour extends beyond the boundary of our solid at these points, and the clipping of the circular contour may make our results less reliable. Additionally, our results for θ_c assume quasistatic, subcritical propagation, but it can be seen from our arrow coloration that our fractures likely reach critical failure by $x = 0.3$. As noted above, our K_{norm} criterion is somewhat conservative, but for $x > 0.7$, K_{norm} is between 6 and 28 times K_{Ic}, which certainly indicates critical failure, during which path prediction is more difficult.

These results suggest a surprising predominance of critical fracture in quarrying, since we have chosen model parameters which may underestimate SIFs compared to mean conditions under hard-bedded glaciers. We choose material parameters for Westerly granite,

which has a relatively high critical fracture toughness of 1.79 MPa·m$^{1/2}$ and applied a mid-range loading pressure of 2 MPa. Our $\sigma_n = 2$ MPa would correspond to a 220 m ice thickness with half of the ice in contact with the bedrock step ($\sigma_I = 2\rho gh$) and a water pressure of 2 MPa, but faster-moving and thicker glaciers can have σ_n approach 6 MPa [2].

Additionally, we have not included horizontal bedding planes in our material, which would be expected for a stepped bed, and it has been shown that K_{Ic} is lower for bedding-plane parallel fractures than bedding-plane normal fractures [9]. Since our results suggest that bed-normal fractures curve to become bed-parallel, we may be overestimating K_{Ic} for our material. Both points suggest that our results may actually underestimate the prevalence of critical fracture in a typical subglacial scenario, which may imply that transient fluctuations in subglacial pressures, rather than crack growth rates, are the rate-limiting process for quarrying, which runs counter to the assumption in the current literature [2],[23],[24].

However, before such conclusions are drawn, the drawbacks of our idealized model must be addressed. If we are to interpret figure (5.3) as a kind of crack propagation vector field, we must establish that our physically evaluated propagation angle θ_c is relatively independent of both the crack path and the crack-tip orientation. In order to take figure (5.3) as indicative of the growth tendency for an arbitrary crack, we must investigate how θ_c varies with crack curvature. This will establish the uncertainty in our data points drawn from straight-line fractures.

5.3   Consideration of curved cracks

The main issue with the prior result (figure (5.3)) is that our conclusions assume that our propagation angles do not depend on the fracture path – if the crack tip is oriented differently, or if the fracture path is curved or kinked rather than straight, by drawing conclusions from figure (5.3), we tacitly assume that this history has no effect on our propagation angle θ_c.

In order to investigate the effect of crack-tip orientation on θ_c, we define a set of progressively curved cracks which begin at the origin and end at $(0.25, -0.4)$ (red circle in fig. (5.3)). We repeat our MTS θ_c evaluation (eq. (2.19)) for a set of curves ranging from highly unrealistic (cyan curve) to aligning with the growth arrows in the previous figure

30

(pink curve). Our fracture shapes with the evaluated propagation directions are shown in the left subplot, colored by curvature (see legend). Since it is difficult to discern between arrows, in the right subplot we show propagation angle with respect to curvature, where we convert θ_c from the crack-tip local coordinates to our global coordinates. Note that, as above (see figure (5.1)), we have defined $\theta = 0$ to be bed-normal and $\theta = 90°$ to be bed-parallel.
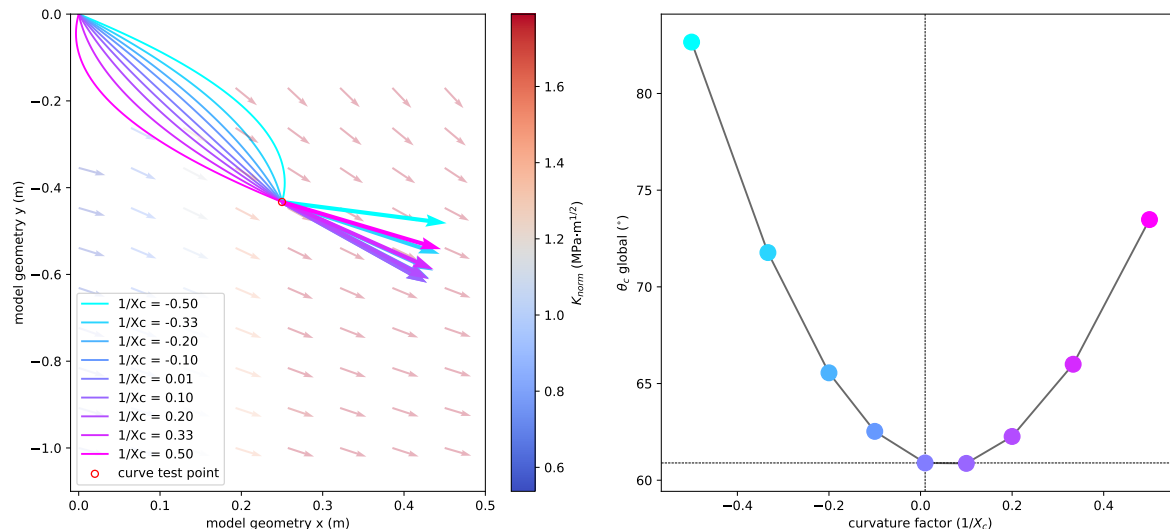

Figure 5.4: Effect of crack curvature on propagation angle θ_c. The traces in the left subplot show a set of curved cracks with shared endpoints, with figure (5.3) underlain. Cracks are colored by curvature, with the evaluated propagation directions indicated by arrows of matching color. In the right subplot, the propagation angles in the global coordinate frame are shown by markers with the same coloration, which goes from an unrealistic curvature $(1/X_c = -0.5)$ to straight $(1/X_c = 0)$ to a realistic curvature $(1/X_c = 0.5)$.

Our results for curvature effect indicate a spread in θ_c of about $20°$ for our full set of cracks. However, the cyan curves are highly unlikely based on figure (5.3), with only our pink curve aligning with our rough vector field. For this more realistic curve, we see about a $13°$ enhancement of the bed-parallel trend we observed in the previous section. This is the main result we intended to verify, and even for our crack angled straight down $(1/Xc = -0.5)$, the propagation angle still points towards the step ledge. If the spread

observed at this point can be generalized to the entire ledge, we predict that free crack propagation simulations would show bed-normal fractures curving to become bed-parallel, and in the meantime progressing partway downwards through the ledge.

Chapter 6

Discussion

Through XFEM simulations of an idealized model for subglacial quarrying, we have arrived at two new insights about this process – (1) a partially-loaded quarter-plane exhibits mixed-mode fracture with a strong mode-II component, and as such has curved, rather than straight-line, fracture propagation; and (2) critical fracture may be widespread in subglacial conditions, and as such fracture propagation may not the rate-limiting factor in quarrying.

Crack curvature implies the average quarried mass per step would be less than previously predicted, since the existing literature assumes rectangular blocks. Curved cracks simplify the dynamical situation somewhat, since a secondary fracture process is not longer required to remove rectangular blocks from the bed. Experimental data on quarrying is sparse, but our prediction of crack curvature agrees with the study by Cohen et al. [25], where a rectangular bedrock block was placed underneath Engabreen glacier and the observed fracture curved towards the step ledge. Work is currently underway to reproduce Cohen's experiment in our model, from which we may be able to draw insights about the understudied area of mixed-mode subcritical fracture.

Additionally, it must be emphasized that our conclusions are drawn from a single point within the model's parameter space, and we have not investigated whether our predictions hold for all step shapes, effective pressures, and ice-bed contact ratios. However, a fracture at the edge of ice-bed contact corresponds to the textbook loading scenario for mode-II fracture, and as such we believe bed-normal fracture will not be observed at that location for any range of model parameters.

This mode-II component may vanish, however, for a fracture placed in the center of a step with greater ice-bed contact. The effect of the step ledge may be reduced, which could correspond to a uniaxial compressive load in an infinite plane, which fractures in mode-I/mode-III and propagates normal to the bed via local buckling. For this reason, fracture placement would also be a useful parameter to investigate in order to determine different paths and rates which could have an effect on the overall dynamics of the process, though in this scenario only fractures along the ice-bed interface are significant.

In past research on subglacial erosion, it is generally assumed that rock fractures propagate along planes of weakness or joints, which are anisotropic phenomena that we have not included in our model. Future work also ought to investigate the effects of jointing and strength heterogeneity in the quarrying problem, which may influence both fracture propagation rates and paths.

Finally, most hard-bedded glaciers do not flow over a staircase-shaped bed with hard ledges, and generally have a complex topography of differently-shaped obstacles. Critical fracture may be predominate in beds with sharp ledges, but subcritical fracture may be widespread in more common bed types, thus reaffirming the importance of assessing mixed-mode subcritical fracture.

Overall, our simulations of the idealized quarrying problem have shown that even this simplified model exhibits unexpected and complex behavior, underscoring the multiple scales of complexity which exist in earth system processes. Further, the subglacial system is a deeply complex coupling of water, ice, and rock processes, in which there is always the question of the sensitivity of conclusions to our uncertainty about the complexities involved in the subglacial bedrock shape and state. If a revised expression for quarrying rate is to be presented, there must be some way in which the idealized system averages out some of the specificities of any existing case.

Bibliography

[1] J. B. Woodard, L. K. Zoet, N. R. Iverson, and C. Helanow, "Linking bedrock discontinuities to glacial quarrying," *Annals of Glaciology*, vol. 60, pp. 66–72, 12 2019.

[2] B. Hallet, "Glacial quarrying: A simple theoretical model," *Annals of Glaciology*, vol. 22, pp. 1–8, 1996.

[3] J. C. Jaeger, N. G. W. Cook, and R. Zimmerman, *Fundamentals of rock mechanics*. John Wiley & Sons, 2009.

[4] C. D. Coman, *Continuum Mechanics and Linear Elasticity*, vol. 238. Springer Netherlands, 2020.

[5] C.-T. Sun and Z. Jin, *Fracture Mechanics*. Academic Press, 2012.

[6] A. Kassimali, *Structural Analysis*. Cengage, 6th ed., 2019.

[7] Z. Zhuang, Z. Liu, B. Cheng, and J. Liao, *Extended Finite Element Method*. Academic Press, 2014.

[8] R. G. Ahangar and Y. Verreman, "Assessment of mode i and mode ii stress intensity factors obtained by displacement extrapolation and interaction integral methods," *Journal of Failure Analysis and Prevention*, vol. 19, pp. 85–97, 2 2019.

[9] B. K. Atkinson, "Subcritical crack growth in geological materials," *Journal of Geophysical Research: Solid Earth*, vol. 89, 6 1984.

[10] T. Meng, Y. Yue, J. Ma, B. Jiao, H. Niu, L. Wen, and X. Yongbin, "Use of dc voltage fluctuation method to investigate real-time mode i and mode ii subcritical crack growth behavior in gypsum rock," *Engineering Fracture Mechanics*, vol. 234, 7 2020.

[11] S.-H. Chang, C.-I. Lee, and S. Jeon, "Measurement of rock fracture toughness under modes i and ii and mixed-mode conditions by using disc-type specimens," *Engineering Geology*, vol. 66, 10 2002.

[12] H. Wu, J. Kemeny, and S. Wu, "Experimental and numerical investigation of the punch-through shear test for mode ii fracture toughness determination in rock," *Engineering Fracture Mechanics*, vol. 184, pp. 59–74, 10 2017.

[13] Q. Z. Wang, F. Feng, M. Ni, and X. P. Gou, "Measurement of mode i and mode ii rock dynamic fracture toughness with cracked straight through flattened brazilian disc impacted by split hopkinson pressure bar," *Engineering Fracture Mechanics*, vol. 78, pp. 2455–2469, 8 2011.

[14] C. Wu, S. C. Mantell, and J. H. Davidson, "Mixed-mode subcritical crack growth in orthotropic polymers," *Polymer Engineering and Science*, vol. 48, pp. 2216–2223, 11 2008.

[15] F. L. Stazi, E. Budyn, J. Chessa, and T. Belytschko, "An extended finite element method with higher-order elements for curved cracks," *Computational Mechanics*, vol. 31, pp. 38–48, 2003.

[16] H. D. Huynh, M. N. Nguyen, G. Cusatis, S. Tanaka, and T. Q. Bui, "A polygonal xfem with new numerical integration for linear elastic fracture mechanics," *Engineering Fracture Mechanics*, vol. 213, pp. 241–263, 5 2019.

[17] J. Dolbow, N. Moes, and T. Belytschko, "A finite element method for crack growth without remeshing," *International Journal for Numerical Methods in Engineering*, vol. 46, pp. 131–150, 1999.

[18] P. Laborde, J. Pommier, Y. Renard, and M. Salan, "High-order extended finite element method for cracked domains," *International Journal for Numerical Methods in Engineering*, vol. 64, pp. 354–381, 9 2005.

[19] H. Li, J. Li, and H. Yuan, "A review of the extended finite element method on macrocrack and microcrack growth simulations," *Theoretical and Applied Fracture Mechanics*, vol. 97, pp. 236–249, 10 2018.

[20] J. R. Rice, "A path independent integral and the approximate analysis of strain concentration by notches and cracks," *Journal of Applied Mechanics*, vol. 35, 6 1968.

[21] G. Cherepanov, "Crack propagation in continuous media," *Journal of Applied Mathematics and Mechanics*, vol. 31, 1 1967.

[22] T. K. Hellen and W. S. Blackburn, "The calculation of stress intensity factors for combined tensile and shear loading," *International Journal of Fracture*, vol. 11, 8 1975.

[23] N. R. Iverson, "A theory of glacial quarrying for landscape evolution models," *Geology*, vol. 40, pp. 679–682, 8 2012.

[24] S. V. Ugelvig, D. L. Egholm, R. S. Anderson, and N. R. Iverson, "Glacial erosion driven by variations in meltwater drainage," *Journal of Geophysical Research: Earth Surface*, vol. 123, pp. 2863–2877, 11 2018.

[25] D. Cohen, T. S. Hooyer, N. R. Iverson, J. F. Thomason, and M. Jackson, "Role of transient water pressure in quarrying: A subglacial experiment using acoustic emissions," *Journal of Geophysical Research: Earth Surface*, vol. 111, 9 2006.